Landslide monitoring using seismic refraction tomography – The importance of incorporating topographic variations

J S Whiteley[1,2], J E Chambers[1], S Uhlemann[1,3], J Boyd[1,4], M O Cimpoiasu[1,5], J L Holmes[1,6], C M Inauen[1], A Watlet[1], L R Hawley-Sibbett[1,5], C Sujitapan[2], R T Swift[1,7] and J M Kendall[2]

[1] British Geological Survey, Environmental Science Centre, Nicker Hill, Keyworth, Nottingham, NG12 5GG, United Kingdom. [2] School of Earth Sciences, University of Bristol, Wills Memorial Building, Queens Road, Bristol, BS8 1RJ, United Kingdom. [3] Lawrence Berkeley National Laboratory (LBNL), Earth and Environmental Sciences Area, 1 Cyclotron Road, Berkeley, CA 94720, United States of America. [4] Lancaster Environment Center (LEC), Lancaster University, Lancaster, LA1 4YQ, United Kingdom [5] Division of Agriculture and Environmental Science, School of Bioscience, University of Nottingham, Sutton Bonington, Leicestershire, LE12 5RD, United Kingdom [6] Queen's University Belfast, School of Natural and Built Environment, Stranmillis Road, Belfast, BT9 5AG, United Kingdom [7] University of Liege, Applied Geophysics, Department ArGEnCo, Engineering Faculty, B52, 4000 Liege, Belgium

Corresponding author: Jim Whiteley (jim.whiteley@bristol.ac.uk)

Abstract

Seismic refraction tomography provides images of the elastic properties of subsurface materials in landslide settings. Seismic velocities are sensitive to changes in moisture content, which is a triggering factor in the initiation of many landslides. However, the application of the method to long-term monitoring of landslides is rarely used, given the challenges in undertaking repeat surveys and in handling and minimizing the errors arising from processing time-lapse surveys. Using the results of a recent, novel, long-term seismic refraction monitoring campaign at an active landslide in the UK, a simple method for producing a reliable time-series of inverted seismic velocity cross-sections is presented in a workflow. Potential sources of error include those arising from inaccurate and inconsistent determination of first-arrival times, inaccurate receiver positioning, and selection of inappropriate inversion starting models. At our site, a comparative analysis of variations in seismic velocity to real-world variations in topography over time shows that topographic error alone can account for changes in seismic velocity of greater than ±10% in a significant proportion (23%) of the data acquired. The seismic velocity variations arising from real material property changes at the near-surface of the landslide, linked to other sources of environmental data, are demonstrated to be of a similar magnitude. Over the monitoring period we observe subtle variations in the bulk seismic velocity of the sliding layer that are demonstrably related to variations in moisture content. This highlights the need to incorporate accurate topographic information for each time-step in the monitoring time-series. The goal of the proposed workflow is to minimize the sources of potential errors, and to preserve the changes observed by real variations in the subsurface. Following the workflow produces spatially comparable, time-lapse velocity cross-sections formulated from disparate, discretely-acquired datasets. These practicable steps aim to aid the use of the seismic refraction tomography method for the long-term monitoring of landslides prone to hydrological destabilization.

Keywords

seismic refraction, geophysical monitoring, active landslides, topographic change, hydrogeophysics

1. Introduction

The implementation of robust and appropriate monitoring strategies is critical for the ongoing assessment of potentially destabilising processes in landslide systems (Angeli et al., 2000). Near-surface geophysical methods are increasingly used to monitor the subsurface conditions of landslides susceptible to hydrological destabilization (Perrone et al., 2014, Whiteley et al., 2019), most commonly by active-source DC electrical resistivity (ER) (e.g., Lucas et al., 2017) and passive-source seismic monitoring (e.g., Walter et al., 2012). ER can provide information on the moisture dynamics of an unstable slope, and passive-source seismic can provide information on the kinematics of failure events. One major advantage of active-source geophysical methods, such as ER, is their ability to produce spatially high-resolution, time-lapse images of the subsurface. However, the majority of seismic landslide monitoring campaigns utilise passive-source methods, which provide superior temporal resolution, but are limited in their spatial resolution due to practical limitations on the number of sensors in an array.

Seismic refraction tomography (SRT), an active-source seismic method, can characterize the spatial heterogeneities in elastic properties of materials in landslide systems (e.g., Uhlemann et al., 2016). SRT determines the travel-time of artificially generated seismic waves, to build up a series of travel-time curves for waves propagating through the subsurface. These travel-times are inverted to produce subsurface cross-sections of seismic velocity. The two types of body waves used in SRT, P-waves and S-waves, propagate through subsurface media differently depending on lithological and physical properties. P-wave velocity, V_p, is given by

$$V_p = \sqrt{\frac{K+\frac{4}{3}G}{\rho}}, \qquad (1)$$

in which K is the bulk modulus (a measure of a material's resistance to uniform compression), G is the shear modulus (a measure of a material's resistance to shear strain) and ρ is material density. The S-wave velocity, V_s, is given by

$$V_s = \sqrt{\frac{G}{\rho}}. \qquad (2)$$

In solid rock, the relationship between seismic velocity and saturation has been empirically demonstrated, and is relatively well understood. Considering a fully saturated rock, as liquid (with a higher K; Equation 1) in pore spaces initially become replaced by gas, V_p decreases rapidly and V_s changes with saturation due to changes in bulk density and shear modulus (Equation 2) (Wyllie et al., 1956). These seismic attributes and their relationship to the petrophysical properties of rock can be used to determine the effects of saturation on seismic velocity (e.g., Biot, 1956, Gassmann, 1951).

In soils, the effect of variations in saturation on seismic velocity is less well-understood. Existing evidence indicates that both the distribution of moisture throughout the soil structure, as well as the influence that capillary forces have on effective pressure, influence V_p at small scales (Romero-Ruiz et al., 2018). Experiments in artificial, well-mixed, homogenous soils, have demonstrated that V_p decreases with increasing saturation (Lu and Sabatier, 2009) and similar results have been obtained from laboratory measurements on undisturbed samples of Loess soils (Flammer et al., 2001). These decreases in V_p are dominated by changes in the matric potential of the soil (related to capillary forces). The effects of capillary forces are likely to be very different between artificial and natural soils, with the former having no internal structure or little consolidation, both of which reduce the influence of capillary forces.

Despite this lack of understanding on the precise mechanism by which seismic velocities are influenced by moisture content in soils, seismic attributes are still routinely used in larger scale field studies to assess characteristics of near-surface sediments. The ratio between V_p and V_s (V_p/V_s) can be used to assess lithology, strength and quality, structure and saturation of near-surface sediments for geotechnical investigations (Bhowmick, 2017). Seismic surveys to obtain in-situ V_p, V_s and V_p/V_s have been used to image physical properties, including ground saturation, in the field (Pasquet et al., 2016b), and have been used to monitor shallow saturation processes in the laboratory (Pasquet et al., 2016a). Poisson's ratio, a property closely related to V_p/V_s ratio which measures lateral strain to axial strain, has been shown to relate to porosity in near-surface sediments, and can be used to determine areas of localised saturation (Uhlemann et al., 2016, Uyanık, 2011).

The use of SRT as a tool for long-term landslide monitoring is almost absent from the literature. Examples of active-source seismic landslide monitoring campaigns focus on the characterization of surface fissures (see Grandjean et al., 2009, Bièvre et al., 2012) rather than the monitoring of moisture-induced elastic property variations. The dearth of studies using SRT as a long-term monitoring tool for landslides is likely due to the complexity of managing and minimizing the several sources of error in the individual surveys (i.e., time-steps) that comprise a monitoring time-series. In this study, we present the results of acquiring, processing and inverting a long-term SRT time-lapse dataset collected from an active landslide. To our knowledge, the use of SRT in a monitoring campaign at an active landslide site has not been implemented to date. The methodology is applied to time-lapse SRT monitoring at a site of active slope failure in North Yorkshire in the UK. This study aims to develop a practical approach to active-source time-lapse seismic surveying of vulnerable slopes, and to demonstrate the applicability of high spatial resolution subsurface monitoring using SRT. The approach taken is summarised in a workflow, from which a practical walkthrough of how the time-lapse SRT data were acquired, processed and inverted using a novel two-stage inversion procedure is presented. The importance of incorporating the topography of the landslide surface from every survey (i.e., for each time-step) in a monitoring campaign is highlighted. Summary results from the SRT monitoring campaign are presented and discussed, and support the use of SRT to monitor moisture dynamics at active landslide sites. The approach and results of this study should be of interest to researchers studying the evolution of subsurface processes acting to destabilise landslide systems (Jaboyedoff et al., 2019), and to those using geophysical methods in landslide early-warning systems (Intrieri et al., 2012) and monitoring environmental changes.

2. Seismic refraction tomography monitoring at the Hollin Hill Landslide Observatory

The Hollin Hill Landslide Observatory (HHLO) in North Yorkshire, UK (Chambers et al., 2011, Merritt et al., 2013), is operated by the British Geological Survey. The landslide comprises an interbedded series of Lower and Middle Jurassic sandstones and mudstones (Figure 1), namely the Whitby Mudstone Formation (WMF) and Staithes Sandstone Formation (SSF).

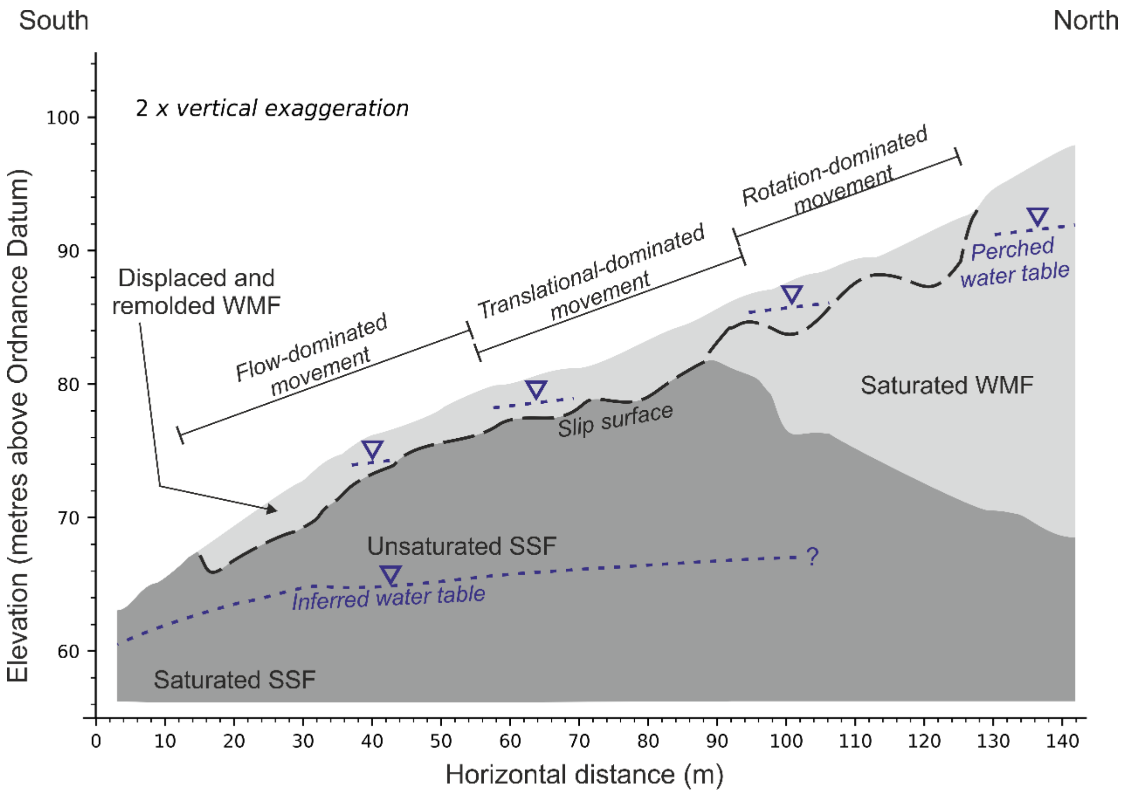

Figure 1: A simplified conceptual model of the HHLO (modified from Uhlemann et al., 2016), indicating movement domains, slip-surface, indicative positon of water tables, and main lithological units comprising the Whitby Mudstone Formation (WMF) and Staithes Sandstone Formation (SSF).

The moisture content of the WMF controls displacement occurrence at the site. The WMF is of low permeability and drains slowly into the underlying SSF. Hence, during periods of increased precipitation, moisture content within the WMF increases quickly (creating localized perched groundwater tables), and decreases slowly during periods of lower precipitation. Slope failure is most likely during these periods of intense and prolonged rainfall.

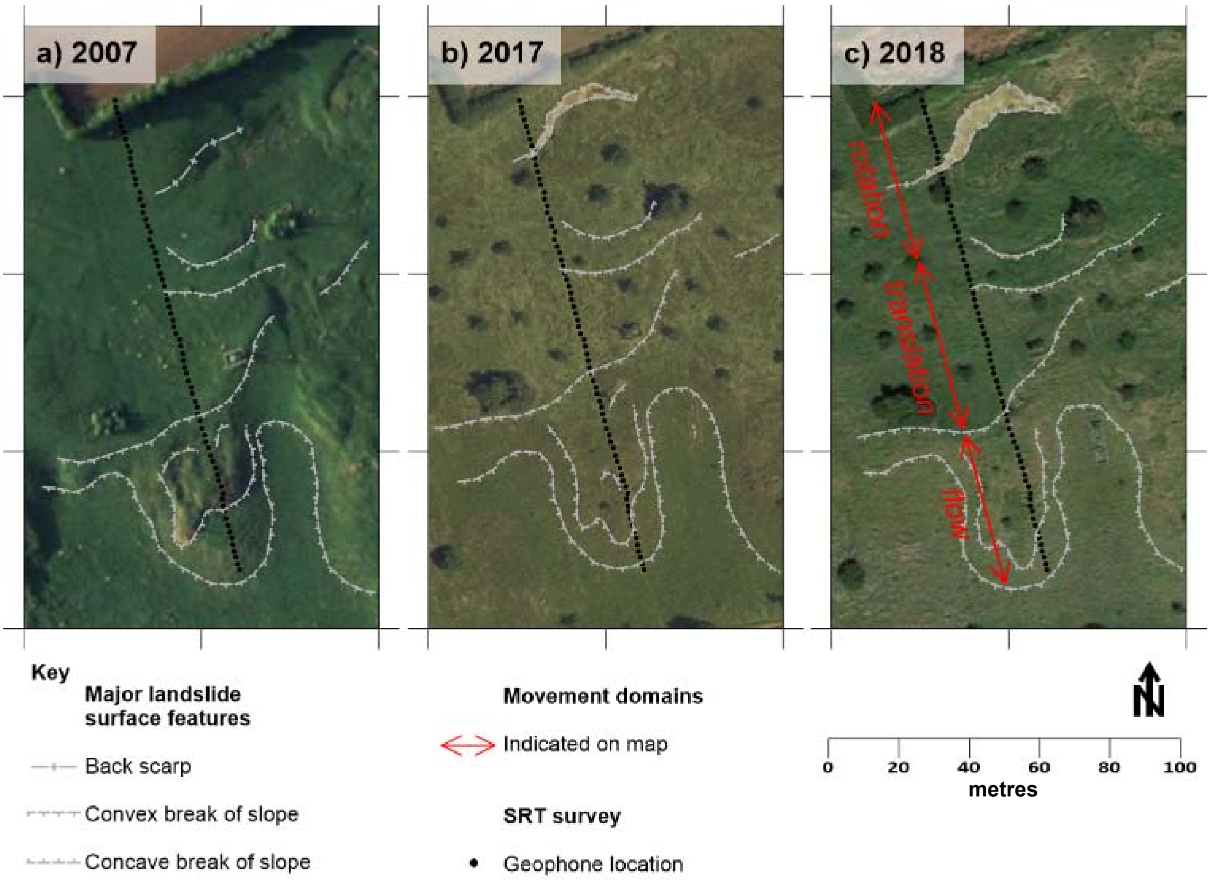

Figure 2: Aerial photographs from the Hollin Hill Landslide. a) Image from 2007 showing the main features of the landslide, including backscarps at top of slope (north), and flow-lobes at base of slope (south). Map data: Google, Infoterra Ltd and Bluesky. b) Image from 2007 showing development of new backscarp after movement in 2016. Map data: Digimap. c) Continued backscarp development shows landslide extension, and propagation of the backscarp to the west. Map data: Google. Black dots are the indicative locations of receivers used in the SRT surveys, with the first receiver location (northern most dot) located outside of the active landslide area, acting as a static reference point against which the receiver arrays are deployed. The location of this receiver is marked by a ground peg installed at the site.

Seasonal variations in moisture content, linked to regional groundwater levels and local infiltration of rainwater, decrease restraining soil-suction forces (potentially producing destabilising positive pore-water pressures) initiating movement at the slip-surface mid-slope. This translational displacement propagates uphill as support for overlying material is removed, culminating in the development and widening of rotational backscarps in the saturated WMF at the top of the slope. Downslope, mobilised material is reworked to form flow lobes at the base of the landslide, where movement is eventually arrested through drainage to underlying deposits of well-sorted, aeolian quaternary sands deposited at the top of the SSF. Aerial imagery from 2007, 2017 and 2018 shows the development of geomorphological landslide features at the HHLO (Figure 2).

SRT monitoring at the HHLO aims to identify changes in the elastic properties of the underlying lithological units. These variations in elastic properties are primarily driven by variations in slope moisture dynamics. Between October 2016 and August 2019, 16 SRT surveys were acquired, resulting in the production of 16 V_p and 16 V_s cross-sections spanning a period of 1001 days, close to 33 months.

The length of time of the monitoring period allowed data to be collected over two distinct annual climatic cycles, ensuring data were acquired at different subsurface moisture contents, and during multiple wetting and drying phases of the landslide system, capturing temporal heterogeneity in hydrological condition. Data were acquired at an average return interval of 9 weeks, which was deemed to be practicable given the characteristics of the landslide system and long-term monitoring period. A shorter return interval would have been desirable, but this was prevented by the logistical and financial cost of mobilisation, equipment availability and deployment, and acquisition and processing time associated with each survey; surveys typically involved two to three days of fieldwork, followed by several days of data processing.

The SRT surveys were acquired along the same profile location over the duration of the monitoring campaign. The profile comprised of 2m spaced geophones (i.e., receivers), positioned from the crest of the landslide to the toe (Figure 2). The location of the survey profile was chosen based on previous geophysical surveys that have been undertaken at the site (see Uhlemann et al., 2016) and position of geotechnical sensors (see Merritt et al., 2013). For both the P- and S-wave surveys, a 48-channel ABEM Terraloc Mk6 was used to acquire seismic refraction data. To acquire contiguous data from the entire spread length (142m total length, comprising 72 receiver locations), two separate 48 receiver (94m long) profiles with a 46m overlap between the surveys were acquired. Receivers used in both deployments were not moved between spread acquisitions, and shot locations were accurately relocated and repeat shots undertaken, so that the overlapping spreads could be processed as a single profile of data.

Vertical geophones with a dominant frequency of 8Hz were used as receivers for the P-wave survey, and a 4 kg sledgehammer and horizontal steel plate were used as a source. At each shot location, data were recorded for 1 second, in order to acquire both refracted P-wave arrivals and surface wave data (these latter data are not described in this study). Shot records were stacked in the field, and the number of stacked shot records varied between surveys based on environmental conditions, such as wind speed and rain; a minimum of two stacks per location were acquired in optimal conditions (i.e., low or no wind and rain), and up to six stacks per location were acquired in poorer conditions.

For the S-wave survey, horizontal geophones with a dominant frequency of 14Hz were used as the receivers, and a prism with ~45° inclined face was used to generate S-waves in opposing polarisations, perpendicular to the orientation of the receiver profile (Uhlemann et al., 2016). Data were recorded for 0.5 seconds, and same-polarisation shot records were stacked, with a minimum of two stacked per receiver location saved in optimal survey conditions, and up to a maximum of six shot records per location saved in poor survey conditions.

In both surveys, geophones were buried to a depth of ~10cm below ground level in an attempt to isolate the receivers from aerial environmental noise, and to provide better coupling with the subsurface. Shots were acquired at every other receiver location (i.e., every 4 m) for the whole of the receiver spread, starting at the first receiver at the crest of the slope. It was not possible to acquire off-end shots at the top of the profile (i.e., before the first geophone), due to access. For the P-wave surveys, off-end shots at the end of the of the spread were acquired at 4m intervals beyond the penultimate receiver at the toe of the slope to a maximum off-end distance of 22m beyond the last receiver (i.e., 164m from the first receiver). For the S-wave surveys, off-end shots were acquired at 10m intervals to a distance of 20m beyond the last receiver (i.e., 162m from the first receiver). For both surveys, the same shot locations were used throughout the entire monitoring campaign, ensuring consistent spatial coverage between surveys.

3. Overcoming challenges in long-term SRT monitoring of landslides

In this study, several sources of error in SRT surveys need to be accounted for during data acquisition, and in the subsequent data processing and inversion stages. Some of these sources of error are unique to landslide monitoring. The goal during processing is to minimize transient changes in time-lapse data that may arise from differences in survey set-up and processing of data between surveys, and to preserve changes arising from genuine variations in the properties of landslide materials. As velocity is the quotient of distance and time, the determination of accurate velocities relies on correct picking (i.e., identifying correct travel-times) and positioning (i.e., determining true distances) of data. The major sources of potential error in SRT acquisition and processing are related to:

Data quality and processing

- Consistent picking of first-arrivals
- Consistent coverage of data
- Development of an appropriate error model

Topographic and inversion parameters

- Consistent repositioning of receivers to the same locations between surveys
- Capturing variations in receiver positions between surveys
- Accounting for changes in landslide topography between surveys

Appropriate inversion constraint

- Incorporating errors into the inversion
- Determining appropriate constraints for data inversion
- Using constraints to regularize data over time

A workflow to produce a robust seismic velocity time-series is shown in Figure 3. The following sections describe how the stages of the workflow are used to address the issues outlined above.

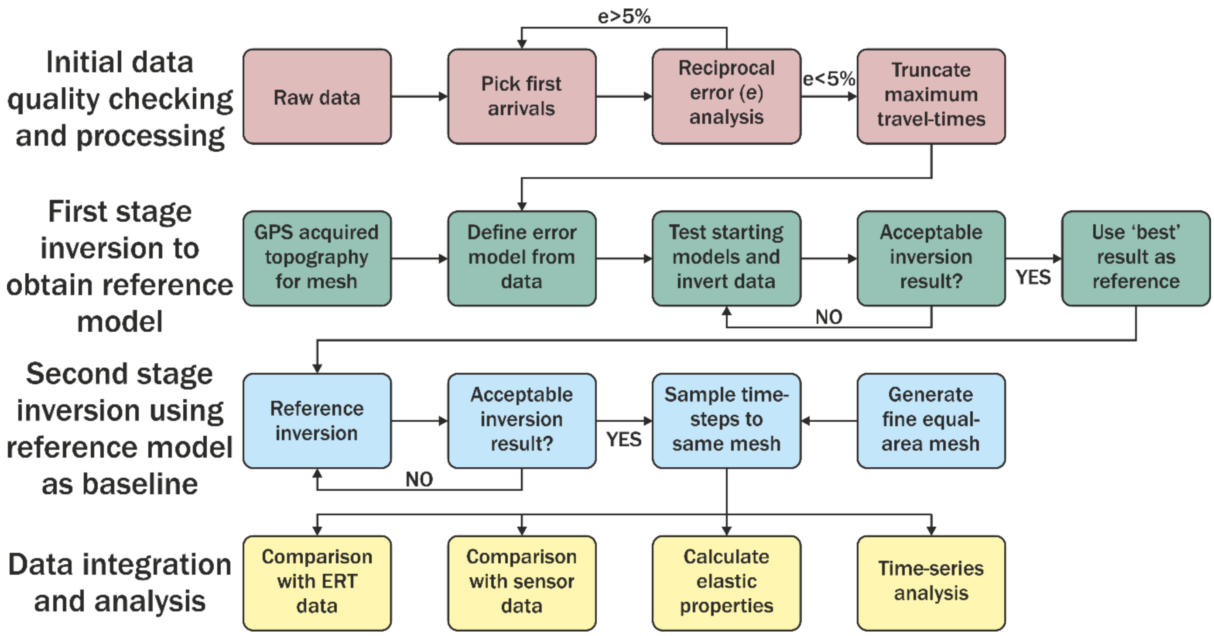

Figure 3: Proposed workflow for processing SRT surveys to produce time-lapse data. SRT data are first processed using reciprocal data analysis for quality control. Individual SRT datasets are inverted for velocity models using a reference model approach. Time-lapse SRT images are then created using unique topography acquired at each survey, in order to determine velocity changes in the subsurface between surveys.

3.1. Data quality and processing

Identifying consistent, repeatable first arrivals in SRT data is a recognised challenge with no universally accepted solution. Attempts include using automatic picking algorithms (e.g., Khalaf et al., 2018) and using statistical approaches (e.g., Dangeard et al., 2018) to minimize absolute and relative errors introduced by operators picking time-lapse SRT data. In this study, reciprocal errors between inverse source-receiver configurations are used to identify 'bad' picks that display an unacceptable differential in reciprocal travel-time. Reciprocal measurements require receiver locations to be used as both receiver and source location during the course of the survey. Therefore, reciprocal analysis is undertaken on ~50% of the entire data for any given survey, and is used as a representative sample of the entire survey dataset i.e., a reciprocal error subset. The error (e) in a reciprocal measurement (defined as the mean travel-time of the two measurements) is defined as

$$|e| = 100 \cdot \left(\frac{|\,t_n - t_r|}{t_n + t_r}\right), \tag{4}$$

in which t_n is the travel-time between a source at position A, and receiver at position B, and t_r is the travel-time between a source at position B and a receiver at position A. Lack of measurement reciprocity occurs when intra-survey (i.e., within the same time-step) data coverage is inconsistent. Factors leading to poor data coverage include low signal-to-noise-ratio at larger source-receiver offsets and interference from noise sources, such as wind, rain and amplification of these noise sources through nearby trees (Figure 4a). Lack of reciprocity occurs in travel-times with further source-receiver offsets, and therefore the use of reciprocal measurements as a data quality indicator favors data acquired from the very near-surface (i.e., shots with smaller source-receiver offsets). Across all of the reciprocal error subsets from each time-step in this study, 12.5% of the V_p data and 14.1% of the V_s data are not analysed due to lack of reciprocal measurements. Remaining reciprocal-pairs of measurements showing a discrepancy *e*>5% are re-examined and re-picked (Figure 4b). Shot records adjacent to a reciprocal-pair with *e*>5% are also considered during this procedure. The data are then re-analyzed, and any further measurements with *e*>5% are re-picked. This iterative process continues until all measurements in the dataset have *e*<5%.

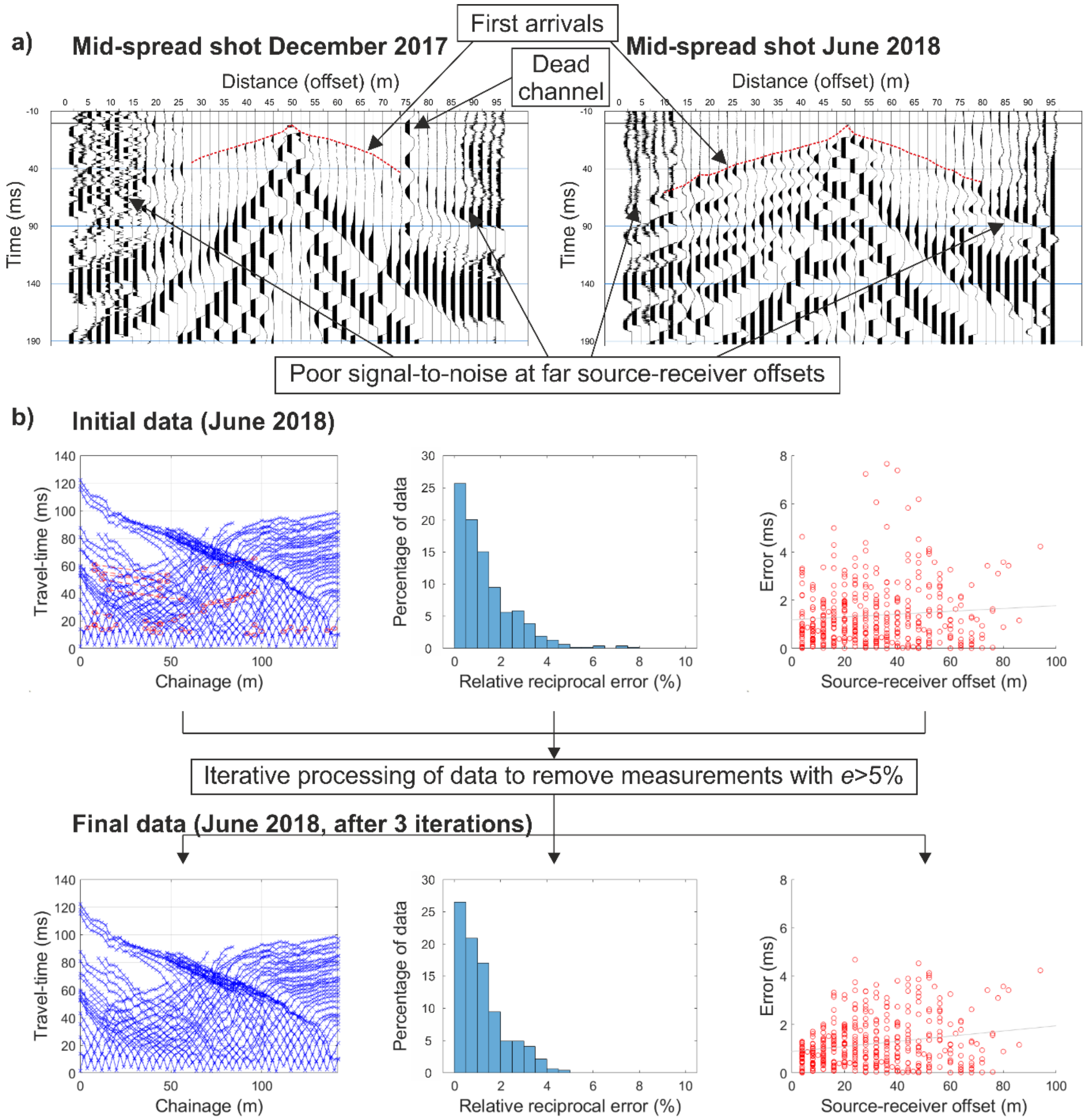

Figure 4: a) Examples of V_p *shot records from the same position at the HHLO from December 2017 (left panel) and June 2018 (right panel). Poor signal-to-noise at larger source-receiver offsets prohibits the identification of first arrivals, and prevents acquiring reciprocal pairs for every measurement in the survey. b) The process of identifying reciprocal errors within a subset of the refraction survey data with* e*>5% from* V_p *data from June 2017. Top left panel shows all first-arrival data (displayed as travel-time curves) with pairs of measurements of* e*>5% circled in red. Top centre panel shows the distribution of relative reciprocal errors within the reciprocal error data subset, and the top right panel shows the distributions of absolute reciprocal errors from this data subset as a function of source-receiver offset, indicating that shots with further offsets have*

higher errors. The corresponding panels below show the effect of iteratively identifying and re-picking data with e>5%, in order to reduce errors across the dataset.

A further issue arising from implementing a time-lapse approach is achieving consistent inter-survey (i.e., between time-steps) data coverage over time. Consistent coverage could not always be achieved due to variations in noise sources between surveys. Surveys showed a significant variation in maximum recorded travel-times, and without some normalisation of these maximum travel-times, comparison of the inverted sections to determine an appropriate reference model (see Section 3.3) is challenging, primarily due to differences in maximum travel-times inducing significant variations in the maximum depths of coverage in the inverted models. To overcome this, the distribution of all travel-times from across the monitoring period is plotted, and a travel-time value that preserves the majority of the data is chosen as a cut-off. In this case, the chosen cut-off travel-times are 86ms and 178ms for the V_p and V_s data, respectively. Data with travel-times over this cut-off are discarded, creating consistency in coverage between time-steps, but reducing the total number of data points. Across all of the time-steps of this study, 1.5% of the V_p data and 17.1% of the V_s data are discarded, giving a common maximum travel-time between surveys. More V_s data are discarded due to better to signal-to-noise ratios during the V_s surveys, giving better data quality and coverage, but in turn requiring larger amounts of data to be discarded to match the coverage of the V_p surveys.

3.2. Topography and inversion parameters

Repositioning of receivers to repeatable x, y and z positions on the landslide surface is crucial to ensure that seismic ray paths are sampling comparable domains of the subsurface over time. The positioning error in x and y can be minimized by deploying receivers relative to permanent markers located outside of the active area of the landslide, and recording absolute x and y positions for receiver locations. Furthermore, the slope surface (z) will change between surveys. This effect cannot be removed by accurate positioning, and therefore needs to be incorporated into the data processing. Variations in z, as well as small unavoidable discrepancies in x and y positions can be captured using accurate geodetic surveying methods.

In this study, receivers are deployed every 2m, with the first receiver located outside of the active landslide area (i.e., above the backscarp) and deployed at the same absolute position for each survey. A permanent ground peg marks the location of this first receiver, and a tape measure draped across the ground surface is used to deploy the remainder of the survey profile relative to this location. A Real-Time Kinetic Global Navigation Satellite System (RTK-GNSS) is used to capture the absolute positions in x, y and z of all receivers with a precision <0.05 m. With accurate positional data for each survey, the 'line-of-sight' distance (d) between one receiver location with coordinates (x_i,y_i,z_i) and another with coordinates (x_{i-1},y_{i-1},z_{i-1}) can be expressed as

$$d_i = \sum_1^i \sqrt{(x_i - x_{i-1})^2 + (y_i - y_{i-1})^2 + (z_i - z_{i-1})^2} \quad . \tag{3}$$

Topographic features between these receiver locations (i.e., those features smaller than the receiver spacing) are not captured in the data.

For accurate 2D seismic travel-time inversion, accurate elevations and horizontal distances of the receivers are required, as the fundamental problem to be solved is one of distance and time. It is common in SRT surveys (and in array-type geophysical surveys in general) for the elevations (z_i) of sensors to be recorded accurately, but for the inter-receiver spacing to be assumed to be a “fixed” nominal horizontal distance. This is particularly common in surveys on flat or uniformly dipping surfaces, where accurate inter-receiver spacing are easier to measure and control. However, in environments where topography can vary sharply within the receiver array, such as landslides, this approach can lead to errors in the positioning of receivers, which in turn introduces errors in to the generation of subsurface meshes for inversion, ultimately influencing the resulting inverted travel-times. Figure 5 shows the discrepancies that can arise from assuming a “fixed” nominal spacing (e.g., assuming receivers are deployed every 2m, without accounting for the changes in distance that topography will create) with variable z_i measurements (red points) against using the true x_i, y_i and z_i positions to generate line-of-sight distances using Equation 3 in this study (green points). Using a “fixed” nominal spacing for time-lapse monitoring ignores lateral variations in receiver spacing, and results in an overestimation of array length. Acquiring topographic information at every survey (i.e., time-step) allows for accurate inversion of travel-times.

The SRT profile is orientated to match the maximum slope profile, which is broadly parallel to the north-south orientation, and therefore the main direction of recorded wave propagation for the SRT survey was also in a north-south direction. Greater variations in the y coordinate of the receiver position (i.e., north-south orientation, parallel to slope) would therefore introduce larger errors to the results of the seismic survey if not accounted for, as opposed to variations in x coordinates (i.e., east-west orientation, perpendicular to slope), which have a smaller effect. Between each survey, the mean variation in receiver repositioning is 0.03m in the x coordinate (1.5% of receiver spacing), and 0.01m in the y coordinate (0.5% of receiver spacing), which is below the nominal accuracy of the equipment used for data acquisition. Across the entire monitoring period (26 months), receiver positions vary by an average of 0.41m in the x coordinate (20.5% of receiver spacing) and 0.15m in the y coordinate (7.5% of receiver spacing). Some active areas of the landslide experience much greater variations due to changes in the slope displacements (Figure 5).

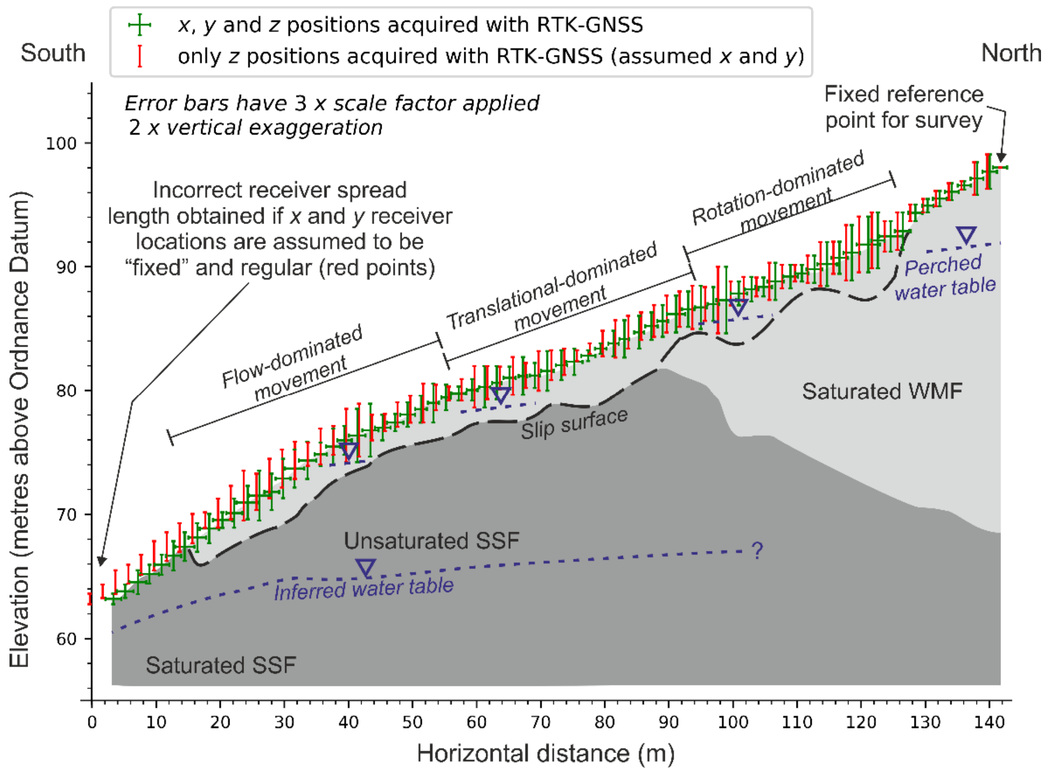

Figure 5: The positions of receivers used in the SRT surveys at HHLO superimposed on to the site conceptual model, and their variation over the monitoring period. The green points are surveyed positions using an RTK-GNSS system, where Equation 3 has been used to generate true line-of-sight receiver distances. The red points show how errors in positioning can arise if a "fixed" nominal receiver spacing is assumed, resulting in lateral erros in receiver positions, and over-estimation of slope length.

3.3. Appropriate inversion parameters

In this study, 2D inversion of the seismic data is undertaken using the open-source Python based software *pyGIMLi* (Rücker et al., 2017). This software allows the inclusion of an error model derived from the absolute and relative errors across the entire time-lapse dataset, obtained by determining the slope and intercept of a linear best-fit line of absolute errors plotted against mean reciprocal travel-time (both in milliseconds). A mesh-generation module in *pyGIMLi* produces unique meshes for each time-step inversion, derived from the RTK-GNSS measurements (see section 3.2). The production of unique meshes for each time-step increased intra-survey accuracy, but presents issues for later time-series analysis; in an ideal monitoring campaign, the inversion meshes for each of the survey time-steps would be identical, allowing for comparison of inverted velocity models on a cell-by-cell basis. However, given the overriding importance of capturing the differences in receiver positions and topography between time-steps, the use of unique meshes is necessary, and this issue is addressed after the final data inversion.

For this study, a two-stage 'reference model' inversion approach is used to constrain the inversion and minimize differences between time-steps (Figure 3). In the first stage, stand-alone inversions of all of the individual time-steps are undertaken, using a variety of constraints for the starting model, including depth, velocity gradient and smoothing factor (Table 1). RMS and chi-squared (χ^2) values are calculated for each inverted model. The 'best-fit' model is assessed by looking at the divergence of χ^2 from a 'perfect-fit' model, in which $\chi^2 = 1$. The model with the lowest absolute divergence (i.e., closest to $\chi^2 = 1$) is designated as the 'reference model' for the second inversion stage. Details of the values of χ^2 and diversion from χ^2 for each inversion are shown in (see Table 2, in Appendix).

In the second stage of the inversion process, the inversion of the entire data set is then repeated, but this time using the 'reference model' from stage one as the starting model, and keeping all other applicable starting model parameters the same as those used in the first stage. Using this method gives all time-steps a realistic and common starting model that is appropriately constrained and represents the local subsurface seismic properties.

Inversion settings							
Inversion parameter	**Depth of mesh**	**Minimum velocity at surface**	**Maximum velocity at base**	**Smoothing factor (lambda)**	**Maximum travel time**	**Absolute data error**	**Relative data error**
P-wave inversion input value	40m	300m/s	3000m/s	25	86ms	0.0242ms	0.02%
S-wave inversion input value	40m	100	1500	25	178ms	0.0194ms	0.006%

Table 1: The inversion parameters used for both stages of the inversion process, for both the V_p *and* V_s *surveys.*

As a result of incorporating unique topography for each time-step, each time-step has a different mesh. To allow for consistent analysis of inverted velocity models between time-steps, the data are re-sampled and interpolated to a regular, refined, triangular mesh (constructed using the same *pyGIMLi* module), effectively creating a spatially-identical time-series on a consistent mesh (Figure 7a). We use a mesh generated with the most recent topography in the monitoring campaign, in order to better reflect an up to date state of the system. One consequence of this approach is that some cells from earlier surveys, in which the surface positions may now have slipped downslope are not sampled to the resampling mesh. To mitigate against this effect, we use a refined cell size that is smaller than the original cells used for the inversion, purposefully oversampling the inverted data in order to discretize the subsurface, and capture variations in the very near-surface. This enables a range of analyses of the time-lapse dataset (see Figure 3; Data analysis and integration).

4. Topographic induced variations in seismic velocity

In section 3.2, we emphasise the importance of accurately capturing the intra-survey topography by using 2D line-of-sight distances from 3D GNSS surveys, and using topography data acquired for each individual survey in the monitoring campaign. This short section serves to demonstrate how failing to accurately capture variations in topography can have a significant impact on final inverted V_p and V_s measurements.

To demonstrate the effect of temporal topographic variation on seismic velocity, the first 14 V_p datasets (D_0:D_{13}) and accompanying topographic surveys (T_0:T_{13}) are processed according to the workflow in Figure 3, and the text in Sections 3.1 to 3.3. A P-wave travel-time dataset from midway through the

monitoring campaign, January 2018 (D_8), is processed and inverted using the surveyed topography (T_8) to produce a 'true' time-step dataset (TTS_8) comprising 2128 subsurface V_p data points. The same seismic dataset (D_8) is then processed using the remaining topographic data (T_0:T_7, T_9;T_{13}), resulting in 13 SRT time- steps with 'false' topography (FTS_0:FTS_7, FTS_9:FTS_{13}). The variations present in these 'false' time-steps represent the effect that real-world variations in topography across the monitoring period have on seismic velocity. By normalising all of the time-step data to TTS_8, the results from January 2018 become a baseline against which variations in seismic velocity arising from subtle, but realistic changes in landslide topography are assessed. The result of this analysis is shown in Figure 6. They indicate that topographic variations can have a large impact on the resulting V_p, with 23% of the total data showing velocities greater than ±10% of the true maximum recorded velocity. This has significant implications when trying to identify variations arising from genuine subsurface elastic property changes caused by environmental factors, as these variations can be very subtle (see Section 5).

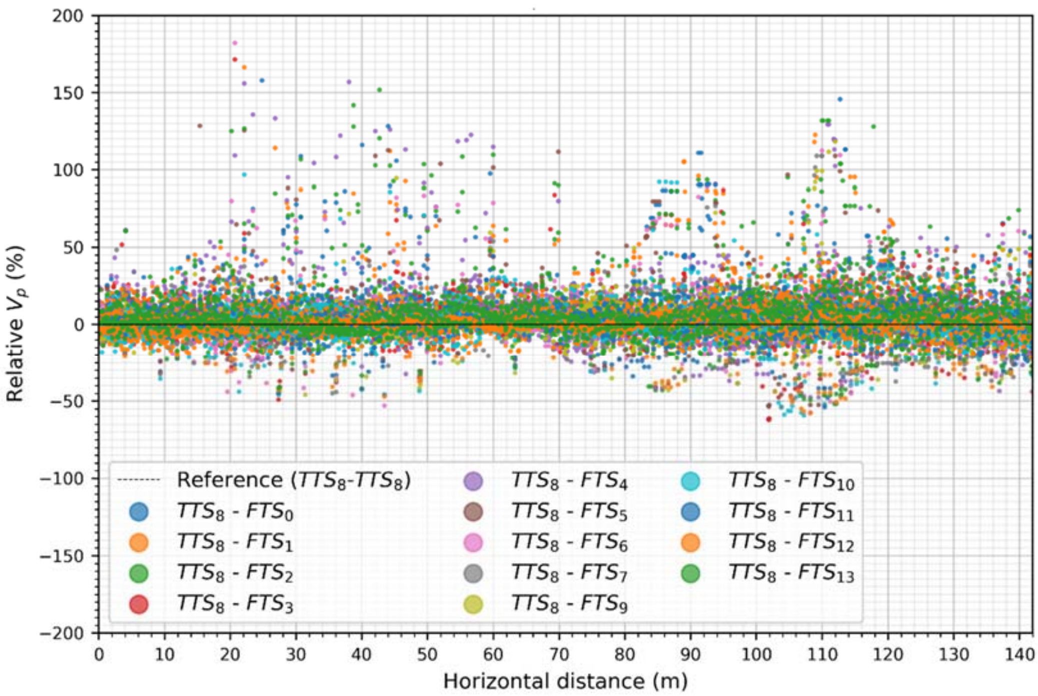

Figure 6: Relative changes in V_p *caused by subtle, real-world changes in topography. The solid black line at* y=0 *represents a normalised baseline (*TTS_8*-*TTS_8*). The same seismic dataset (*D_8*) has been processed using the other time-step topographic data; any variations in* V_p *are therefore a product of these subtle topographic changes between surveys.*

5. Data analysis and results

One approach to analysing time-series SRT data is to look at how the seismic attributes of discrete seismic units respond to changing environmental conditions. The prevalent subsurface lithological discontinuities (i.e., those that are stable in time) are highlighted by plotting the mean values of the individual cells across the 33 month monitoring period (Figure 7). These plots are displayed using the most recent topography in the time-series. The individual cross-sections highlight significant subsurface features, including changes in lithology at depth, and different domains

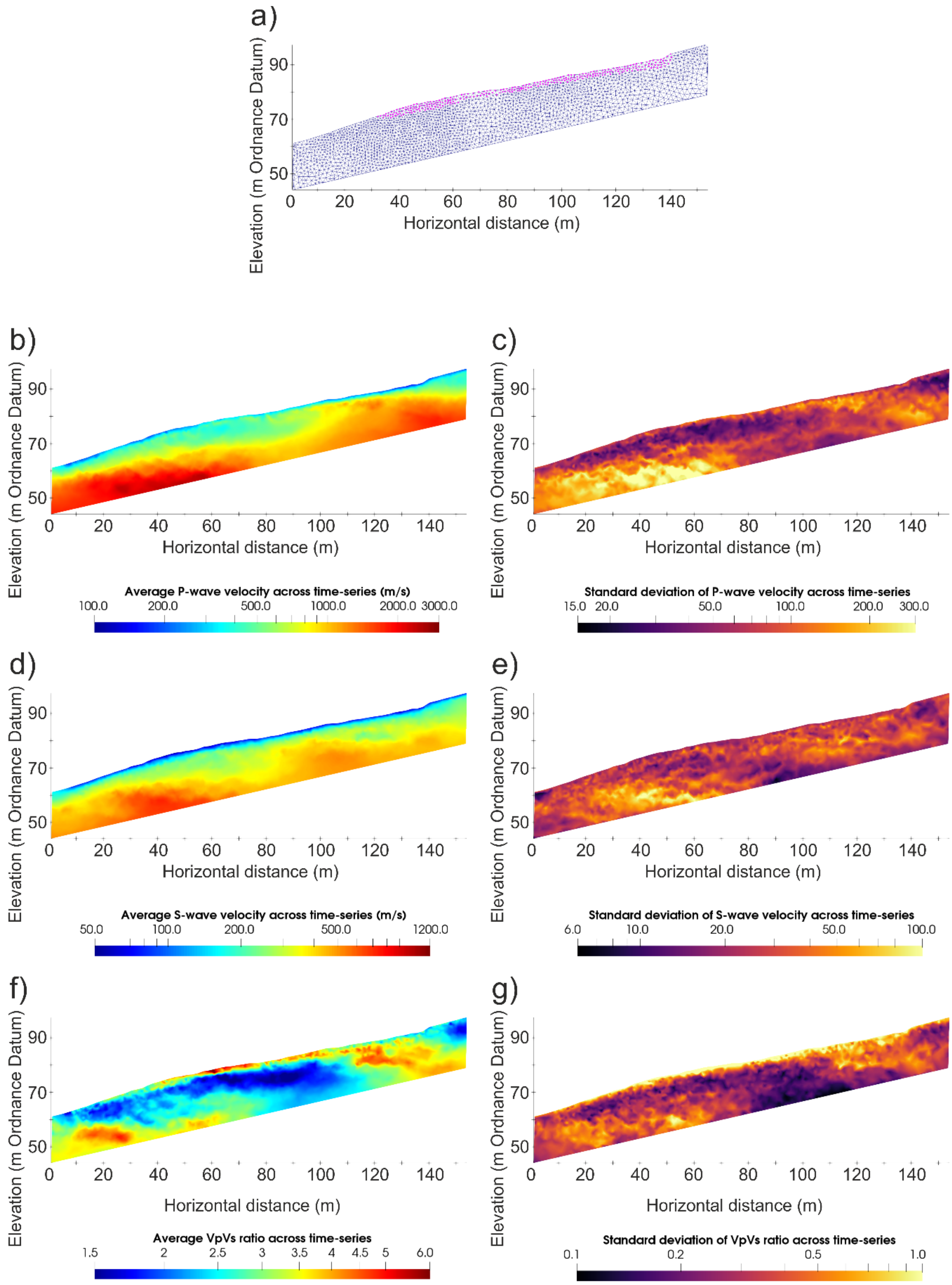

Figure 7: a) The regular mesh used to sample all of the individual time-steps to create spatially comparable datasets for the time-series. The cells highlighted purple in the surface sliding have been used for the analysis in Figure 8. b) Cross-section

showing average V_p *across the time-series. The value shown in each cell (see Figure 7a) is the mean velocity value from the entire 26 month monitoring period. c) Cross-section showing average* V_s *across the time-series. The value shown in each cell (see Figure 7a) is the mean velocity value from the entire 26 month monitoring period. d) Cross-section showing average* V_p/V_s *across the time-series. The value shown in each cell (see Figure 7a) is the mean ratio value from the entire 26 month monitoring period.*

of movement in the near surface. Plots showing the standard deviation of these mean values (Figure 7) indicate the areas of the landslide that show greatest velocity variation across the monitoring period.

Here we concentrate on the sliding layer at the HHLO (extending from the surface to 2 – 4m depth), which is easily identified by the low V_p and V_s at the surface of the cross-sections. This extends from beneath the break in slope at the bottom of the back scarp (~15m horizontal distance), to the base of the flow lobes (125m horizontal distance). At HHLO this surface sliding layer is monitored by several subsurface and surface environmental sensors, recording rainfall and changes in moisture content, allowing direct comparison with inverted cross sections. By selecting grid cells within this layer, it is possible to calculate the change in velocity over time. In our case, the surface layer comprises grid cells from both the V_p and V_s time-series datasets (Figure 7b and Figure 7d), the positions of which are fixed through the use of a common fixed mesh. Figure 8 shows the time-series V_p and V_s inverted values extracted from this surface layer, alongside calculated effective rainfall, soil moisture data from a cosmic-ray sensor measuring shallow (~0.1m bgl) moisture content across the site. V_p increases and decreases in relation to soil moisture, but with a time lag. The lag effect is caused by the difference of the sampling depth of the moisture sensor (<0.1m bgl) and the depth of the V_p readings (2 – 4m bgl); the moisture content of the HHLO near-surface changes more quickly in relation to net infiltration and evapotranspiration rates (shown by the hourly soil moisture, faint green line) than the top 2 – 4m of the landslide, which will be less subject to evapotranspiration processes at depth. It is also worth noting that inverted velocities will be smoothed values from the true velocities, due to the spatial and temporal smoothness constraints used.

Furthermore, the calculated V_p/V_s ratio (Figure 7f), which is an indicator of material saturation (Uyanık, 2011), better reflects changes in moisture content. Crucially, the minimum V_p (350 m/s) in the time-series is 24% less than the maximum V_p (462 m/s). Given that topographic effects alone can cause variations in V_p >±10%, the changes in seismic velocity over time could easily be masked if the data are not processed correctly. This demonstrates the necessity for including accurate topography in long-term SRT monitoring campaigns in landslide settings.

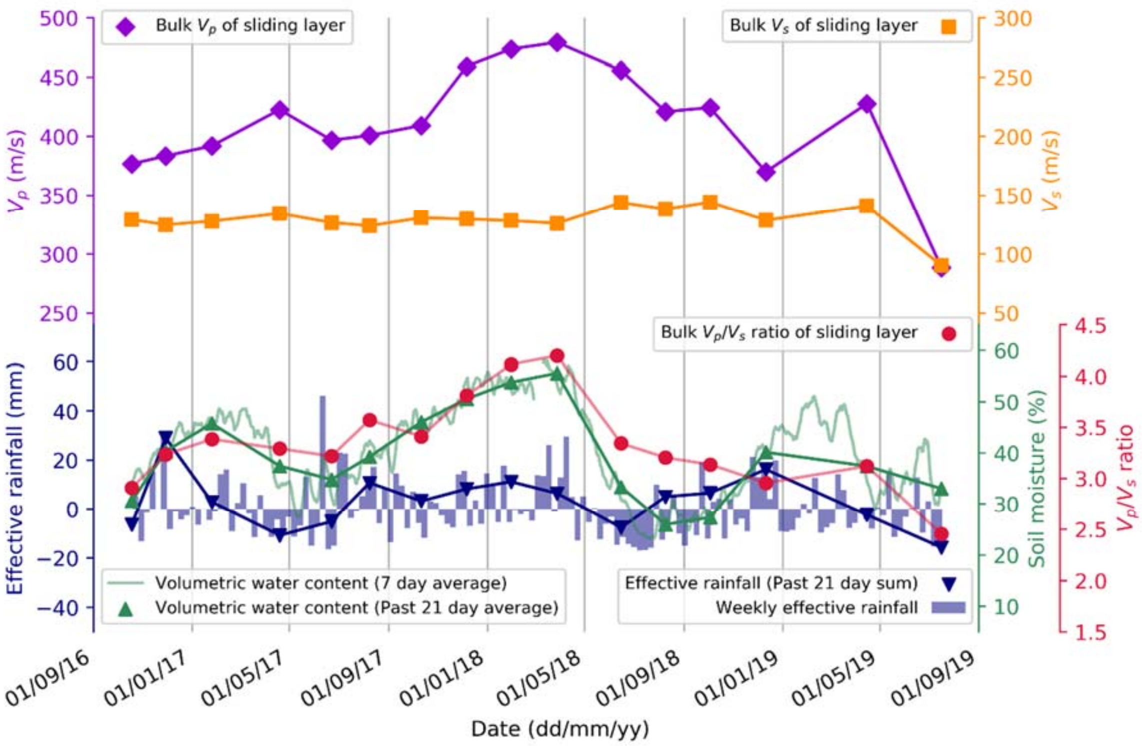

Figure 8: The top panel shows variation in bulk V_p and V_s *readings from the sliding layer at the HHLO (see Figure 7 for location of this layer). The shaded areas are the 1st and 3rd quartiles of the range in* V_p and V_s*. The* V_p/V_s *s ratio, derived from the bulk* V_p and V_s *readings is shown. In the bottom panel, weekly effective rainfall, showing periods of net infiltration/evapotranspiration at the HHLO, and soil moisture from a surface sensor measuring to <0.1m bgl. The variation in* V_p *broadly follows the increases and decreases in moisture content, while* V_s *shows little variation. The derived* V_p/V_s *s ratio shows greatest sensitivity to the moisture content of the surface sliding layer at HHLO.*

6. Conclusions

SRT is rarely used for the long-term assessment of landslides prone to hydrological destabilization, but has much potential for high-resolution spatial monitoring. Landslide monitoring campaigns using SRT can determine seismic attributes of slipped materials, which provides information on elastic property changes due to temporal variations in moisture content. However, failing to give due attention to the possible sources of error in SRT surveys can lead to artefacts in the time-lapse data, which can easily mask changes arising from genuine variations in the elastic properties of landslide materials, including the underlying rock. We have shown how velocities in the near-surface soil layers are sensitive to variations in moisture content, but we also provide a workflow for addressing the errors associated with SRT.

Standard approaches to quality assessing and processing SRT data aid in minimizing intra-survey error. The use of emerging methods to increase picking accuracy, such as automatic detection algorithms, machine learning and statistical approaches will also decrease the errors introduced in to the creation of time-lapse data from standalone surveys. For the dataset considered here, data from each survey were processed using reciprocal error analysis to ensure e<5% of travel-time for all datasets. However, in the case of producing time-lapse data from these individual datasets, we underscore the importance of using detailed, unique topography data for processing each time-step. This crucial step could easily be overlooked by inaccurate assumptions regarding field setup, receiver spacing landslide surface movement between surveys, even by experienced SRT operators.

For the dataset considered here, changes in topography lead to >±10% variations in apparent seismic velocities in 23% of the data for the unconsolidated near-surface. Our data exhibits a 24% difference between the fastest and slowest V_p observed in this layer, underscoring the need to properly account for topography effects. To avoid the errors associated with changes in topography, accurate source-receiver positions are important when processing SRT monitoring data. Several other steps, including the repositioning of receivers in the field, the use of data quality indicators (such as travel-time reciprocity) and robust reference models for inversion further reduces these errors. If these potential sources of error are managed correctly, SRT presents a useful tool for the identification of heterogeneous subsurface conditions and their changing properties over time in active landslide settings.

Acknowledgements

The authors would like to acknowledge Florian Wagner for advice on the *pyGIMLi* API. We would also like to acknowledge members, students and visiting scholars of the BGS' Geophysical Tomography team for their input and support. This work was funded by a NERC GW4+ UK Doctoral Training Partnership Studentship (Grant NE/L002434/1) and in part by the BGS University Funding Initiative (S337), which are gratefully acknowledged. Jim Whiteley and Jonathan Chambers publish with the permission of the Executive Director, British Geological Survey (UKRI-NERC).

References

Angeli, M.-G., Pasuto, A. & Silvano, S. 2000. A critical review of landslide monitoring experiences. *Engineering Geology,* 55**,** 133-147.

Bhowmick, S. 2017. Role of Vp/Vs and Poisson's Ratio in the Assessment of Foundation(s) for Important Civil Structure(s). *Geotechnical and Geological Engineering,* 35**,** 527-534.

Bièvre, G., Jongmans, D., Winiarski, T. & Zumbo, V. 2012. Application of geophysical measurements for assessing the role of fissures in water infiltration within a clay landslide (Trièves area, French Alps). *Hydrological Processes,* 26**,** 2128-2142.

Biot, M. A. 1956. Theory of Propagation of Elastic Waves in a Fluid-Saturated Porous Solid. I. Low-Frequency Range. *The Journal of the Acoustical Society of America,* 28**,** 168-178.

Chambers, J. E., Wilkinson, P. B., Kuras, O., Ford, J. R., Gunn, D. A., Meldrum, P. I., Pennington, C. V. L., Weller, A. L., Hobbs, P. R. N. & Ogilvy, R. D. 2011. Three-dimensional geophysical anatomy of an active landslide in Lias Group mudrocks, Cleveland Basin, UK. *Geomorphology,* 125**,** 472-484.

Dangeard, M., Bodet, L., Pasquet, S., Thiesson, J., Guérin, R., Jougnot, D. & Longuevergne, L. 2018. Estimating picking errors in near-surface seismic data to enable their time-lapse interpretation of hydrosystems. *Near Surface Geophysics,* 16**,** 613-625.

Flammer, I., Blum, A., Leiser, A. & Germann, P. 2001. Acoustic assessment of flow patterns in unsaturated soil. *Journal of Applied Geophysics,* 46**,** 115-128.

Gassmann, F. 1951. *Über die Elastizität Poröser Medien*.

Grandjean, G., Hibert, C., Mathieu, F., Garel, E. & Malet, J.-P. 2009. Monitoring water flow in a clay-shale hillslope from geophysical data fusion based on a fuzzy logic approach. *Comptes Rendus Geoscience,* 341**,** 937-948.

Intrieri, E., Gigli, G., Mugnai, F., Fanti, R. & Casagli, N. 2012. Design and implementation of a landslide early warning system. *Engineering Geology,* 147**,** 124-136.

Jaboyedoff, M., Del Gaudio, V., Derron, M.-H., Grandjean, G. & Jongmans, D. 2019. Characterizing and monitoring landslide processes using remote sensing and geophysics. *Engineering Geology***,** 105167.

Khalaf, A., Camerlynck, C., Florsch, N. & Schneider, A. 2018. Development of an adaptive multi-method algorithm for automatic picking of first arrival times: application to near surface seismic data. *Near Surface Geophysics,* 16**,** 507-526.

Lu, Z. & Sabatier, J. M. 2009. Effects of Soil Water Potential and Moisture Content on Sound Speed. *Soil Science Society of America Journal,* 73**,** 1614-1625.

Lucas, D. R., Fankhauser, K. & Springman, S. M. 2017. Application of geotechnical and geophysical field measurements in an active alpine environment. *Engineering Geology,* 219**,** 32-51.

Merritt, A. J., Chambers, J. E., Murphy, W., Wilkinson, P. B., West, L. J., Gunn, D. A., Meldrum, P. I., Kirkham, M. & Dixon, N. 2013. 3D ground model development for an active landslide in Lias mudrocks using geophysical, remote sensing and geotechnical methods. *Landslides,* 11**,** 537-550.

Pasquet, S., Bodet, L., Bergamo, P., Guérin, R., Martin, R., Mourgues, R. & Tournat, V. 2016a. Small-Scale Seismic Monitoring of Varying Water Levels in Granular Media. *Vadose Zone Journal,* 15.

Pasquet, S., Holbrook, W. S., Carr, B. J. & Sims, K. W. W. 2016b. Geophysical imaging of shallow degassing in a Yellowstone hydrothermal system. *Geophysical Research Letters,* 43**,** 12,027-12,035.

Perrone, A., Lapenna, V. & Piscitelli, S. 2014. Electrical resistivity tomography technique for landslide investigation: A review. *Earth-Science Reviews,* 135**,** 65-82.

Romero-Ruiz, A., Linde, N., Keller, T. & Or, D. 2018. A Review of Geophysical Methods for Soil Structure Characterization. *Reviews of Geophysics,* 56**,** 672-697.

Rücker, C., Günther, T. & Wagner, F. M. 2017. pyGIMLi: An open-source library for modelling and inversion in geophysics. *Computers & Geosciences,* 109**,** 106-123.

Uhlemann, S., Hagedorn, S., Dashwood, B., Maurer, H., Gunn, D., Dijkstra, T. & Chambers, J. 2016. Landslide characterization using P- and S-wave seismic refraction tomography — The importance of elastic moduli. *Journal of Applied Geophysics,* 134**,** 64-76.

Uyanık, O. 2011. The porosity of saturated shallow sediments from seismic compressional and shear wave velocities. *Journal of Applied Geophysics,* 73**,** 16-24.

Walter, M., Arnhardt, C. & Joswig, M. 2012. Seismic monitoring of rockfalls, slide quakes, and fissure development at the Super-Sauze mudslide, French Alps. *Engineering Geology,* 128**,** 12-22.

Whiteley, J. S., Chambers, J. E., Uhlemann, S., Wilkinson, P. B. & Kendall, J. M. 2019. Geophysical Monitoring of Moisture-Induced Landslides: A Review. *Reviews of Geophysics,* 57**,** 106-145.

Wyllie, M. R. J., Gregory, A. R. & Gardner, L. W. 1956. Elastic wave velocities in heterogeneous and porous media. *Geophysics,* 21**,** 41-70.

Appendix

See below.

P-wave inversions																	
Stage one inversion results																	
Time-step	**-**	**0**	**1**	**2**	**3**	**4**	**5**	**6**	**7**	**8**	**9**	**10**	**11**	**12**	**13**	**14**	**15**
χ2	-	0.982	1.495	1.952	1.345	1.478	1.138	1.434	1.358	1.848	1.573	1.288	1.316	1.258	0.982	1.157	0.992
RMS	-	2.970	3.788	4.971	4.310	4.143	4.412	4.721	5.244	5.713	5.431	4.010	3.965	3.727	3.404	4.157	3.492
χ2 divergence		0.018	0.495	0.952	0.345	0.478	0.138	0.434	0.358	0.848	0.573	0.288	0.316	0.258	0.018	0.157	0.008
Stage two inversion results																	
Time-step	**Reference (best fit model from stage one)**	**0**	**1**	**2**	**3**	**4**	**5**	**6**	**7**	**8**	**9**	**10**	**11**	**12**	**13**	**14**	**15**
χ2	0.992	0.984	1.516	1.904	1.486	1.593	1.440	1.733	1.445	2.238	1.893	1.442	1.351	1.357	1.161	1.330	0.927
RMS	3.492	3.157	3.935	4.860	4.466	4.069	5.044	4.729	5.202	5.693	5.515	4.314	3.966	4.050	3.987	4.148	3.385
χ2 divergence	0.008	0.016	0.516	0.904	0.486	0.593	0.440	0.733	0.445	1.238	0.893	0.442	0.351	0.357	0.161	0.330	0.073
S-wave inversions																	
Stage one inversion results																	
Time-step	**-**	**0**	**1**	**2**	**3**	**4**	**5**	**6**	**7**	**8**	**9**	**10**	**11**	**12**	**13**	**14**	**15**
χ2	-	1.117	1.416	2.061	1.959	2.654	1.991	2.499	1.563	1.771	3.822	1.614	2.873	2.517	1.910	2.179	2.100
RMS	-	1.206	1.415	1.764	1.678	2.001	1.685	1.910	1.491	1.704	1.974	1.716	2.068	1.933	1.629	1.770	1.750
χ2 divergence		0.117	0.416	1.061	0.959	1.654	0.991	1.499	0.563	0.771	2.822	0.614	1.873	1.517	0.910	1.179	1.100
Stage two inversion results																	
Time-step	**Reference (best fit model from stage one)**	**0**	**1**	**2**	**3**	**4**	**5**	**6**	**7**	**8**	**9**	**10**	**11**	**12**	**13**	**14**	**15**
χ2	1.117	0.990	1.520	2.082	1.988	2.629	1.912	2.243	1.713	1.681	1.728	1.812	2.861	2.533	1.913	2.047	2.039
RMS	1.206	1.124	1.479	1.657	1.745	2.018	1.532	1.820	1.731	1.724	1.716	2.349	2.106	2.074	1.612	1.889	1.675
χ2 divergence	0.117	0.010	0.520	1.082	0.988	1.629	0.912	1.243	0.713	0.681	0.728	0.812	1.861	1.533	0.913	1.047	1.039

Table 2: The results of the two-stage inversion process for both the Vp *and* Vs *surveys. In stage one, data are inverted using the parameters in Table 1. The 'best' result is then assessed by looking at divergence from a perfect model fir (i.e., a normalised χ2 value, called χ2 divergence. In both the* Vp *and* Vs *inversions, the first survey (time-step 0) showed the best model fit, and was used for subsequent inversion. In stage two, this best-fit 'reference model' is used as the starting model, and all data are re-inverted against this, providing a real-world starting model for the time-series.*